QUANTUM GASES

Thermography of the superfluid transition in a strongly interacting Fermi gas

Zhenjie Yan¹†, Parth B. Patel¹, Biswaroop Mukherjee¹, Chris J. Vale², Richard J. Fletcher¹, Martin W. Zwierlein¹*

Heat transport can serve as a fingerprint identifying different states of matter. In a normal liquid, a hotspot diffuses, whereas in a superfluid, heat propagates as a wave called "second sound." Direct imaging of heat transport is challenging, and one usually resorts to detecting secondary effects. In this study, we establish thermography of a strongly interacting atomic Fermi gas, whose radio-frequency spectrum provides spatially resolved thermometry with subnanokelvin resolution. The superfluid phase transition was directly observed as the sudden change from thermal diffusion to second-sound propagation and is accompanied by a peak in the second-sound diffusivity. This method yields the full heat and density response of the strongly interacting Fermi gas and therefore all defining properties of Landau's two-fluid hydrodynamics.

eat transport is a ubiquitous phenomenon at work in everything from steam engines to the formation of stars, and it dictates how energy, information, and entropy flow in the system. In conventional materials, heat, mass, and charge are all transported by the motion of (quasi)particles, such as electrons in metals. This common origin of transport results, for example, in the Wiedemann-Franz law, relating thermal and electrical conductivity. However, in strongly correlated systems, such as high-temperature superconductors (1), neutron stars (2), and the quark-gluon plasma of the early universe (3), the notion of a quasiparticle is poorly defined. It is unknown whether there is a common relaxation rate for heat, density, and spin transport (4) or if strong correlations separate these phenomena. Understanding the flow of entropy is at the forefront of current research, with powerful theoretical models connecting thermal flow in quantum systems to gravitational duals (3, 5). Directly measuring thermal transport, as distinct from mass or charge transport, is thus of great relevance for elucidating the origin of heat dissipation in strongly correlated matter.

a Feshbach resonance provide an ideal platform for quantitative studies of fermion transport (6-10). As a result of scale invariance in resonant Fermi gases (11), measurements performed in one system constrain the equation of state and transport properties of other strongly interacting Fermi systems, including neutron matter at densities 25 orders of mag-

Strongly interacting atomic Fermi gases near

¹MIT-Harvard Center for Ultracold Atoms, Research Laboratory of Electronics, and Department of Physics, Massachusetts Institute of Technology, Cambridge, MA 02139, USA. ²Optical Science Centre and ARC Centre of Excellence in Future Low-Energy Electronics Technologies, Swinburne University of Technology, Melbourne 3122, Australia. *Corresponding author. Email: zwierlei@mit.edu. †Present address: Department of Physics, University of California,

Berkeley, CA 94720.

nitude higher. The system features the largest superfluid transition temperature T_c , relative to its density, of all known fermionic systems (12).

In this study, we introduce a thermography method to image heat in interacting quantum gases. The method requires only a temperaturedependent spectral response that can be locally resolved. In the case of the Fermi gas that we studied here, the radio-frequency (rf) spectrum is temperature dependent (13, 14). We spatially resolved this spectral response and directly measured heat transport in the strongly interacting Fermi gas.

The nature of heat transport can help distinguish states of matter. In ordinary liquids, heat transport is purely diffusive and governed by thermal conductivity. By contrast, in superfluids, heat propagates as a wave called "second sound." The two-fluid model of superfluidity introduces normal and superfluid components that can move in and out of phase (15, 16). This gives rise to two distinct sound modes, first and second sound, corresponding to a density and an entropy wave (17). The speed of second sound c_2 is a direct measure of the superfluid fraction $\rho_{\rm S}/\rho_{\rm N}$, the ratio of the superfluid density ρ_S to the normal component density ρ_N (18). Its attenuation yields the second-sound diffusivity D_2 , which involves the thermal conductivity, bulk, and shear viscosities (17, 19). Consequently, we observe a dramatic change in thermal transport as the Fermi gas is cooled below T_c . Simultaneously recording the complete density and heat response of the system to a known external perturbation allows us to completely characterize the two-fluid hydrodynamics of the strongly interacting Fermi gas (19, 20).

Previous studies of thermal transport in quantum gases relied on the weak coupling between the density and temperature of the gas (21-24). This allowed the observation of second sound in Bose (25, 26) and Fermi gases (21, 24, 27) but without directly measuring heat propagation. By using a homogeneous box potential formed by light sheets, we observed running and stan Check for waves of second sound, demonstrating m ple reflections of entropy waves from the walls of the box. Our thermography works across the superfluid transition, allowing the observation of a pronounced peak in thermal diffusion at T_c characteristic of critical behavior expected near second-order phase transitions.

Spectral thermometry

The working principle of our method is sketched in Fig. 1, A to D. In rf spectroscopy, interacting atoms are ejected from the many-body system into an initially unoccupied internal spin state (28). For interacting gases, the resulting spectra depend on temperature. At high temperatures, when the thermal de Broglie wavelength is shorter than both scattering length and interparticle distance, the spectra approach the bare, unshifted response for an isolated atom. Conversely, at low temperatures, the spectra display interaction-induced shifts known as "clock shifts." In the particular case of attractive twocomponent Fermi gases, at zero temperature the spectral peak is shifted by approximately the pairing energy $E_{\rm B}$ of fermion pairs (13), and at nonzero temperature, broken pairs contribute to the response at lower frequencies (Fig. 1A). For a fixed detuning ω_0 on the flank of the spectrum, the rf response is sensitive to changes in temperature (Fig. 1B). As the rf response can be spatially resolved, this allows for a direct measurement of the local temperature from a single image of rf-transferred atoms.

As an exemplary application of this method, we may detect second sound in the fermionic superfluid, which is a wave in the gas of excitations that, close to T_c , consists predominantly of broken pairs (Fig. 1C). A suitably detuned rf drive can transfer atoms from the gas of excitations, yielding a direct, local measure of heat (Fig. 1D). We stress that the method does not depend on this simplified picture of broken pairs and only relies on the temperature dependence of the rf spectrum. It therefore applies in a wide range of temperatures set by the magnitude of clock shifts, which for the unitary Fermi gas are on the scale of the Fermi temperature (13).

Our experiment began with a uniform fermionic superfluid trapped in a cylindrical box potential whose axial direction is defined as the z axis, formed by an equal mixture of resonantly interacting fermions in the first (1) and third (3) hyperfine state of ⁶Li at a Feshbach resonance (magnetic field, 690 G) (29). The density of $n_0 = 0.75 \ \mu m^{-3}$ per spin state corresponds to a Fermi energy of $E_{\rm F} = h \cdot 10.5 \, \text{kHz}$ and a Fermi temperature of $T_{\rm F} = E_{\rm F}/k_{\rm B} \simeq$ 500 nK, where h is Planck's constant and $k_{\rm B}$ is the Boltzmann constant. To create temperature gradients in the superfluid gas, we resonantly excited a standing wave of second

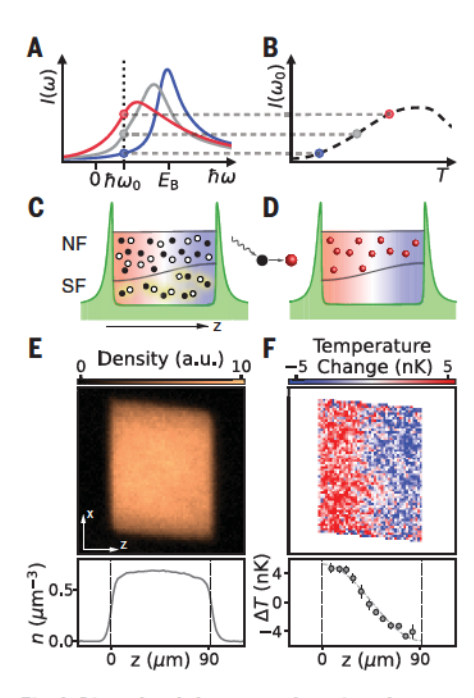


Fig. 1. Direct local thermography using rf spectroscopy. (A) A sketch of rf spectra at various temperatures for the unitary Fermi gas (13). Blue, gray, and red lines correspond to the rf response $I(\omega)$ at successively higher temperatures. (B) At fixed frequency ω_0 on the flank of a spectrum [black dotted line in (A)], the rf response is sensitive to temperature and serves as a local thermometer. (C) In a simplified picture, the superfluid component (SF) consists of fermion pairs, whereas the normal fluid (NF) is composed of broken pairs. (D) The unpaired atoms are transferred to a weakly interacting state by an rf pulse and subsequently imaged to determine the spatial distribution of the normal component density. (E and F) In situ observation of a second-sound wave after resonant gradient excitation. Shown are the column density and local temperature, respectively, from simultaneous in situ absorption images of unperturbed (3) and rftransferred (2) atoms, with density n and temperature variation ΔT , averaged along the x axis, shown below. The vertical dotted line marks the edge of the box potential (half maximum of potential). The black dashed line in (F) is a fit to the fundamental eigenmode in the box [eq. S1 in (18)]. Second sound has a significant effect on the temperature, but not the density.

sound using an oscillating potential gradient along the z axis (Fig. 2A). Our thermography uses rf transfer of atoms from state 1 into the initially unoccupied state $f\equiv 2$. Simultaneous in situ absorption images of atoms in states 2 and 3 along one of the radial direction (y axis) yield the original gas density n(x,z) (Fig. 1E), as well as the density n(x,z) of rf-transferred atoms, carrying the information on the local temperature (Fig. 1F). The rf thermometer is calibrated on gases in thermal equilibrium by

recording the dependence of n_f on temperature, $\frac{\partial n_t}{\partial T}\Big|_n$, and density, $\frac{\partial n_t}{\partial n}\Big|_T$ (18). This method of calibrating spectral responses versus each thermodynamic variable while holding other parameters constant can be applied universally. More generally, all that is required for the observation of thermal transport is access to any local observable that is sensitive to temperature, meaning that it can be achieved even without a calibrated thermometer. Integrating the two-dimensional (2D) temperature profile along the uniform \boldsymbol{x} axis yields a 1D temperature profile, $\Delta T(z)$, the deviation in temperature from the equilibrium state, with a precision of 500 pK from a single image, as shown in Fig. 1F. The data reveal an essentially flat density in the presence of a ~8-nK temperature difference across the box.

Observation of heat propagation

Armed with the ability to spatially resolve temperature in the strongly interacting Fermi gas, we directly observed second sound as the free back-and-forth sloshing of heat after resonant gradient excitation (Fig. 2, B to D). Figure 2B shows the measured temperature variation $\Delta T(\mathbf{x}, \mathbf{z}, t)$ obtained at various times after secondsound generation. Figure 2C presents the time evolution of the 1D temperature profiles $\Delta T(z,t)$, and Fig. 2D shows the corresponding evolution of the amplitude $\Delta T(k_1, t)$ of the first spatial Fourier mode supported by the axial box length $L=91~\mu\mathrm{m}$ ($k_i=j\pi/L$), all clearly demonstrating the wave-like propagation of heat. Here, the absolute temperature of the gas in equilibrium, obtained from expansion (14), was T = 63(2) nK = 0.125(5) T_F , or $T = 0.75(3) T_c$ when compared with the superfluid transition temperature $T_{\rm c} = 0.167T_{\rm F}$ reported in (12). A damped sinusoidal fit to $\Delta T(k_1, t)$ yielded a speed of second sound of $c_2 = \omega/k = 3.57(2)$ mm/s, corresponding to about a tenth of the Fermi velocity $c_2 =$ $0.092(2)v_{\rm F}$. From the measured damping rate Γ , we obtained a diffusivity of second sound $D_2 = \Gamma/k^2 = 2.44(11)\hbar/m$. As was found for the diffusivities of spin (30, 31), momentum (32), and first sound (33), a natural scale for the diffusivity of second sound is reduced Planck's constant $\hbar = h/2\pi$ divided by the particle mass m (27, 34). This scale directly emerges in a strongly interacting quantum fluid from a mean-free path of carriers of approximately one interparticle spacing d, and characteristic speeds of \hbar/md given by Heisenberg's uncertainty (30). A similar scale of diffusivity is also measured for second sound in the strongly interacting bosonic superfluid ⁴He (35), whereas the more weakly interacting fermionic ³He in its superfluid A_1 and B phases displays much larger values that are many hundreds to thousands of times \hbar/m (36).

Thermography provides an unprecedented view of the superfluid transition in the strongly interacting Fermi gas. Figures 2, F and G, show the transition from heat diffusion in the normal state to wave-like propagation of heat, second sound, in the superfluid. For these data, we created a local hotspot on one side of the box by locally applying an intensity-modulated optical grating (Fig. 2E). Modulation at $\sim\!2$ kHz efficiently creates high-frequency phonons that rapidly decay into heat (33, 37), creating a temperature profile with good overlap with the j=1 mode. The subsequent evolution of the temperature amplitude $\Delta T(k_1,T)$ displays a striking change in character from exponential decay above $T_{\rm c}$ to the damped sinusoid of second sound below $T_{\rm c}$.

Entropy and density response functions

The full linear response theory of two-fluid hydrodynamics for superfluids was provided over half a century ago by Hohenberg and Martin (19). Under an external potential that acts on the density n with wave vector k and frequency ω , systems respond through changes in their density n as well as their temperature or equivalent entropy density s Thermography enables us to obtain the corresponding response functions, not only $\chi_{n,n}(k,\omega)$ but also $\chi_{s,n}(k,\omega)$. These encode all the thermodynamic and two-fluid hydrodynamic information of the unitary Fermi gas (18–20).

To determine the linear response functions, we apply a potential gradient, oscillating at frequency ω . The steady-state temperature change $\Delta T(k_1,\omega)$ and density change $\Delta n(k_1,\omega)$, measured after an integer number of oscillation cycles, yield the respective out-of-phase response functions (19, 20). The change in entropy per particle, Δs , is linked to the temperature and density variation by the equation of state. For our scale invariant, unitary Fermi gas, this connection is provided by the specific heat per particle c_V at constant density (11, 12)

$$\Delta s = c_V \left(\frac{\Delta T}{T} - \frac{2}{3} \frac{\Delta n}{n_0} \right) \tag{1}$$

Measurements of fractional temperature and density variations thus directly yield the entropy variation in units of c_V . Figures 3, A and B, display the entropy and density response of the superfluid in a frequency range that solely excites the lowest spatial mode (j = 1), the sloshing mode. The density reveals a dominant peak attributed to first sound near 90 Hz (33) and a faint signature of second sound at 20 Hz, expected in a gas of nonzero expansivity, where density and temperature are coupled. However, in the entropy channel, whose signal derives predominantly from the rf transfer (18), the strong second-sound peak indicates a large response. This directly demonstrates that second sound in the unitary Fermi gas is predominantly an entropy wave, whereas first sound is essentially isentropic. This is similar to the case in superfluid ⁴He

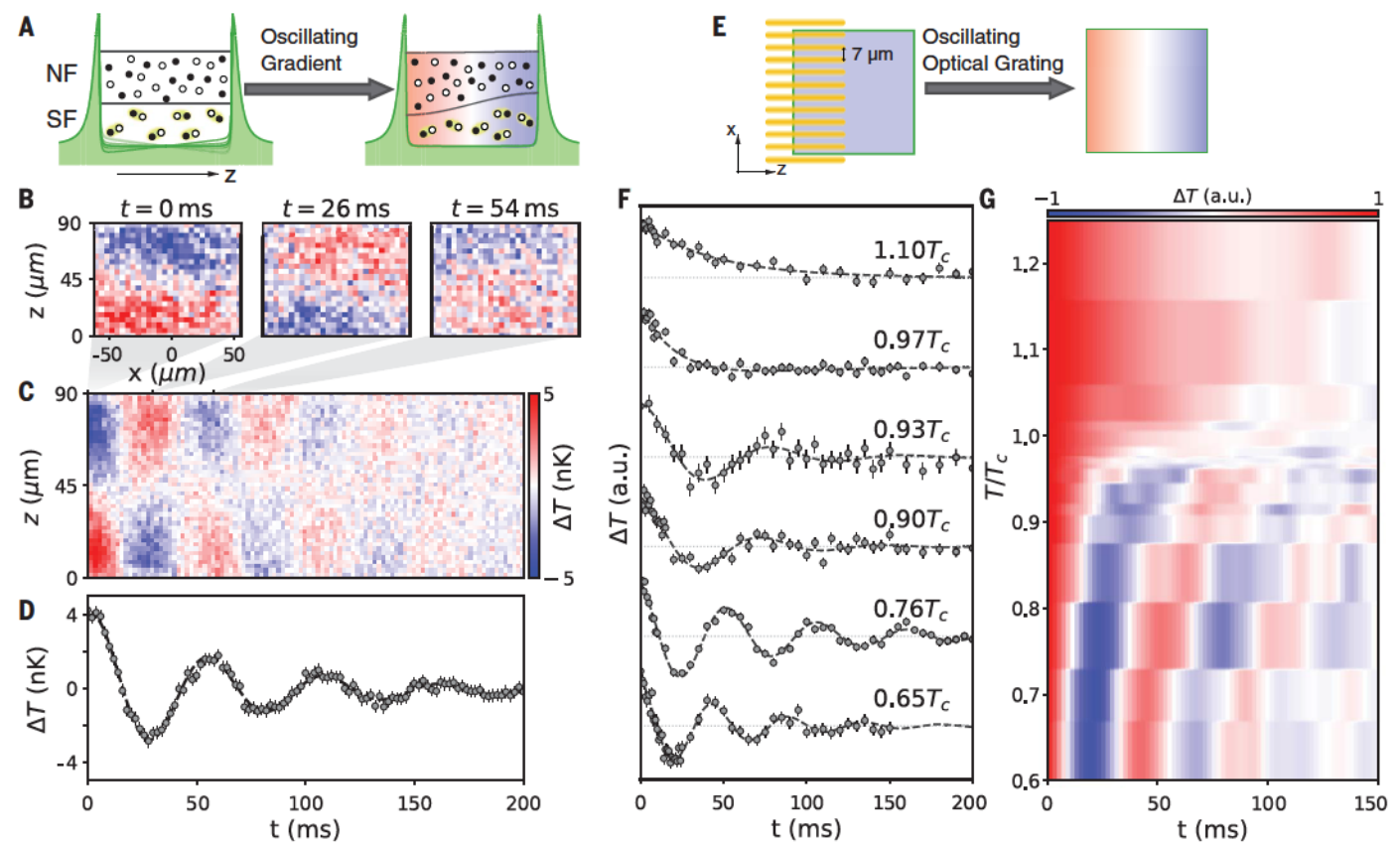


Fig. 2. Direct observation of the superfluid transition from heat propagation in a strongly interacting Fermi gas. (A) Generating second sound with an oscillating potential gradient for data shown in (B) to (D) at a temperature of $T=63\,$ nK or $0.75T_c$. (B) In situ thermographs at times t=0, 26, and 54 ms after second-sound excitation. (C) Time evolution of the axial temperature profiles, revealing the wave-like propagation of heat. (D) Amplitude of the first spatial Fourier mode of the temperature profiles $\Delta T(k_1,t)$ versus time (gray circles). A fit to a damped sinusoid (dashed line) gives the speed and attenuation

rate of second sound. (**E**) Local heating with an intensity-modulated optical grating for data shown in (F) to (G). (**F**) Time evolution of temperature amplitudes $\Delta T(k_1,t)$ (solid circles) and fits (dashed lines) at various gas temperatures. The dotted lines show the $\Delta T=0$ line for each temperature. The fitting method used in (D) and (F) is indicated by eq. S24 in (18). (**G**) Two-dimensional interpolation with Gaussian smoothing of temperature amplitudes versus time across the superfluid transition. In (D) and (E), the initial temperature variation for each time trace is normalized to be 1.

(17) but drastically different from the case in 2D and 3D Bose gases, in which density and entropy are strongly coupled (25, 26, 38). In Figs. 3, C and D, we show the thermal evolution of the entropy and density responses in the first spatial Fourier mode, which serve as a direct measurement of the out-of-phase entropy-density $[\operatorname{Im}\chi_{s,n}(k_1,\omega)]$ and densitydensity $[\operatorname{Im}\chi_{n,n}(k_1,\omega)]$ response functions (18). The measured response functions completely encode all information about the two-fluid hydrodynamics in a unitary Fermi gas (18-20). The peak positions and widths give the speeds and diffusivities of first and second sound. The speed of first sound is a direct measure of the energy of the gas (33), and the speed of second sound yields the superfluid density. The height of the second-sound peak in the entropy-density response is given by the expansivity α_p of the gas, and the weight of the second-sound versus the first-sound response in the density-density response directly equals $\gamma-1$, where $\gamma=c_p/c_V$ is the ratio of heat capacities at constant pressure and density. The thermodynamic quantities α_p and γ are related by the isothermal compressibility κ_T , the heat capacity, and temperature by $\gamma-1=T\alpha_p^2/(n\kappa_Tc_V)$, and in particular for the unitary gas simply by $\gamma-1=\frac{2}{3}\alpha_pT$.

Heat transport across superfluid transition

Figure 4A shows the speed of second sound, measured consistently with our three independent methods: free evolution after resonant excitation of the second-sound mode (yellow squares), local heating (red diamonds), and steady-state response functions (blue circles). The superfluid fraction is obtained from c_2 and the previously measured equation of state (12, 18) and is shown in Fig. 4B. The measurements show a qualitative agreement with Nozières and Schmitt-Rink theory (39, 40) (dotted-dashed line), although their absolute value of T_c differs from experiment. Our super-

fluid fraction agrees well with the result reconstructed for the homogeneous case from the second-sound measurement in a quasi-1D trapped gas in (21), which relied on the same equation of state from (12). With the local heating method (red diamonds), we are able to observe the continuous evolution of c_2 and $\rho_{\rm S}$ from a finite value in the superfluid phase to zero in the normal phase. The phasetransition temperature T_c obtained from this measurement is consistent with the equilibrium thermodynamic measurement (12) (the vertical gray area) and the onset of pair condensation (7, 13), which we have measured here as well (Fig. 4C). As is expected, there is a clear quantitative difference between the superfluid fraction, which saturates to unity at temperatures $T \leq 0.1T_{\rm F}$, and the pair condensate fraction, which remains ≤0.75. The superfluid density quantifies the portion of the fluid that flows without friction. Formally, it measures the rigidity against phase twists,

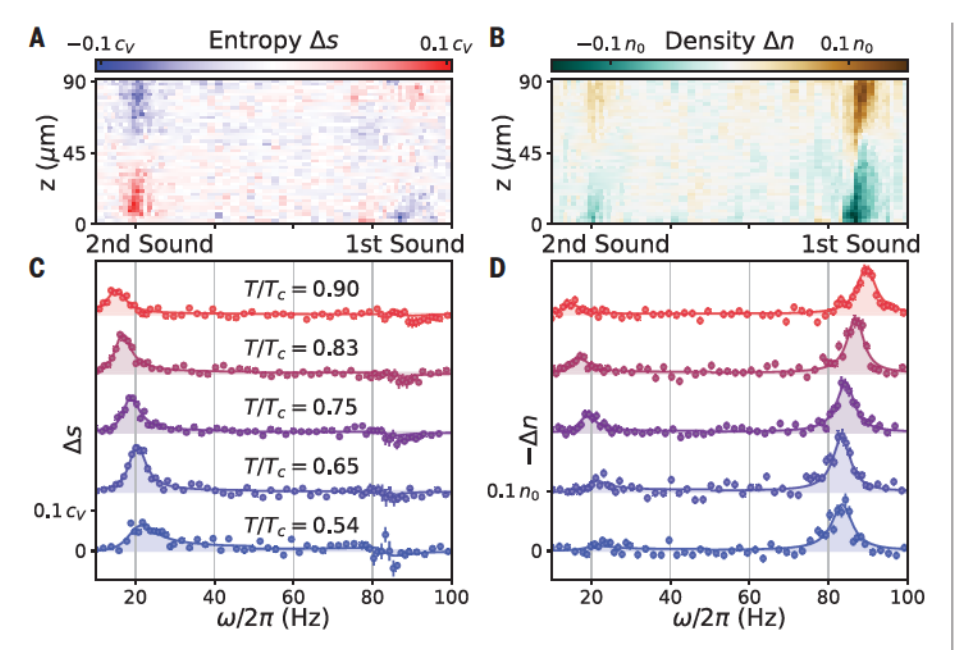


Fig. 3. Steady-state entropy and density response of the unitary Fermi superfluid. Shown are the (A) change in entropy per particle (Δ s) and (B) density (Δ n) after excitation by an integer number of cycles of an oscillating axial potential gradient (Fig. 2E). For frequencies below 50 Hz, the drive duration is 5 cycles at an amplitude of $g = h \cdot 2.12$ Hz/ μ m; for frequencies above 50 Hz, we drive for 20 cycles at an oscillation amplitude of $g = h \cdot 0.85$ Hz/ μ m. The gas temperature is $T/T_c = 0.75$. Amplitudes of the first spatial Fourier mode are shown in (C) and (D) for various temperatures in the superfluid phase. The solid lines are fits using the full entropy- and density-response function from two-fluid hydrodynamics [eqs. S9 and S10 in (18)].

whereas the condensate fraction is a measure for the number of fermion pairs at zero-center of mass momentum. In the zero-temperature limit, the entire system is superfluid, but only a fraction of fermion pairs are condensed, owing to quantum depletion and Pauli blocking (6, 7, 9).

A further dramatic signature of the superfluid transition is seen in the temperature dependence of the second-sound diffusivity D_2 in the superfluid state, and thermal diffusion in the normal state, shown in Fig. 4D. We observe a striking peak in this transport coefficient within a range $\Delta T \approx 0.1T_c$ around the critical temperature of superfluidity, rising above a background minimum value of about $2\hbar/m$ up to nearly three times this value. This behavior echoes that found in liquid 4He (35, 41) near its superfluid transition, associated with classical criticality. Indeed, the order parameters of both the Fermi superfluid and liquid helium belong to the same 3D XY static universality class, and also the same [model F in (42)] dynamic universality class, dictating a behavior $D_2 \propto |T_c - T|^{-v/2}$ near the transition, with critical exponent $v \approx 0.672$, as observed in 4He (41). Related critical behavior for the speed of second sound $c_2 \propto (T_c - T)^{v/2}$ and $\rho_{\rm S} \propto (T_{\rm c} - T)^{\rm v}$ is qualitatively consistent with the steep slopes we observe close to T_c in these quantities. For the unitary Fermi gas, the width of the region governed by criticality is not precisely known but is estimated to be on the order of $T_{\rm c}$ (43, 44). A quantitative analysis of critical behavior, such as the measurement of critical exponents, is prevented by the residual inhomogeneity of the gas density, giving a variation of $\Delta(T/T_{\rm c})\sim 5\times 10^{-3}$, and by the finite size of our system. Indeed, even for the lowest spatial mode j=1, second sound becomes overdamped ($\Gamma\gtrsim 2\omega$) within 3% of $T_{\rm c}$. At low temperatures $T/T_{\rm c}<0.6$, D_2 is again seen to rise significantly, which we attribute to the diverging mean-free path of phonons, the only remaining contribution at low temperatures once pair-breaking excitations are frozen out.

Above the transition temperature, the second-sound mode evolves into a thermal-diffusion mode whose diffusivity is directly given by thermal conductivity κ : $D_2 = \kappa/nc_P$ (19, 20, 45, 46). We therefore find quantum-limited thermal diffusion $\sim 2\hbar/m$ (47), similar to prior results for spin (30, 31), momentum (32), and first-sound diffusion (33) in the unitary gas. However, the nonmonotonous behavior of second-sound diffusivity, with steep rise at low temperatures and around T_c , has not been observed in other transport coefficients.

The second-sound diffusivity D_2 was independently measured with Bragg scattering (27), and a small rise in the second-sound damping rate approaching T_c was observed. However, a peak in D_2 near T_c could not be resolved, pre-

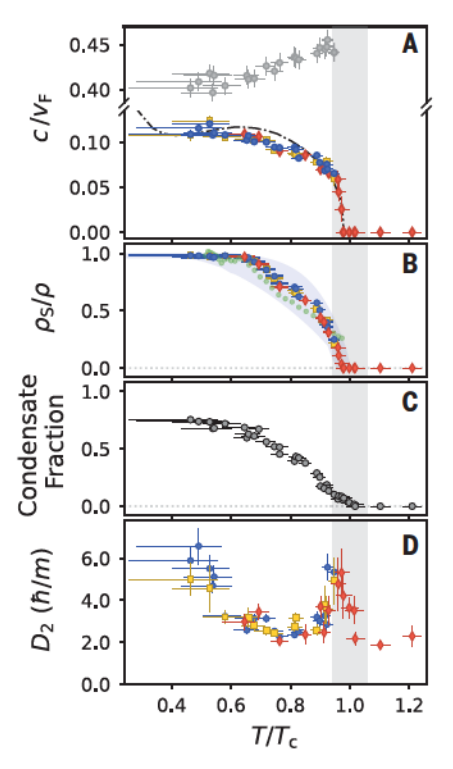


Fig. 4. The speed and diffusivity of second sound. (A) Speed of second sound, normalized by the Fermi velocity, as a function of temperature, determined by fitting the steady-state response functions (blue circles), and the free evolution of second sound after resonant gradient excitation (yellow squares) or after local heating (red diamonds). The first-sound speed measured from the response functions (gray circles) is also shown. The dotteddashed line indicates Nozières-Schmitt-Rink theory (39). (B) The superfluid fraction of the unitary Fermi gas obtained from the speed of second sound [symbols as shown in (A); also see eq. S13 in (18)]. The blue shaded area indicates the uncertainty from the equation of state. Solid green circles indicate the superfluid fraction obtained from quasi-1D experiments (21) that also utilized the MIT equation of state of the unitary Fermi gas (12). (C) Pair condensate fraction measured with the rapid-ramp technique to detect fermion pair condensates (13). (D) Second-sound diffusivity obtained from various methods [symbols as shown in (A)]. The vertical gray area shown in all panels indicates the uncertainty of critical temperature from (12).

sumably because Bragg scattering as a density probe becomes insensitive to heat propagation above T_c . Away from T_c , the values for D_2 reported in (27) were about half of what we observed. Given that the experiment in (27) used a much higher wave vector and correspondingly more elevated frequencies, the gas may no longer have been hydrodynamic but instead entered the collisionless regime, which is similar to the behavior for high-momentum first sound in (33, 37). Assuming the hydrodynamic relation $\Gamma = D_2 k^2$ for such modes will yield

too small a value for D_2 . By contrast, in the present work using thermography, we verified hydrodynamic scaling by exciting also the second (j=2) spatial mode supported by the box, finding within error bars identical values of D_2 [fig. S4 in (18)].

In the superfluid regime of the unitary Fermi gas, there are three contributions to second-sound diffusion: thermal conductivity κ , shear viscosity η , and bulk viscosity ζ_3 from normal-superfluid counterflow (36, 48). Although it is known that $\zeta_3=0$ for a pure phonon gas with linear dispersion (49), in the range $T/T_c \gtrsim 0.5$, the normal fluid is dominated by pair-breaking excitations. In this case, all three contributions are of similar importance (36, 48). Assuming $\zeta_3=0$ in this regime, as was done in (27), is not warranted, and obtaining viscosity and thermal conductivity from first- and second-sound diffusion alone is not possible.

Outlook

Direct measurement of heat transport has been a long-standing goal in quantum gas experiments. Thermography now opens the door to study a host of intriguing nonequilibrium phenomena, from nonlinear heat waves to quench dynamics (50, 51) and even far-from-equilibrium phenomena such as prethermal states (52, 53). Using tomographic imaging techniques (54), the complete 3D spectral response can be measured, enabling the investigation of transverse entropy transport in anisotropic or inhomogeneous systems. For thermodynamic systems with additional degrees of freedom beyond density and temperature, for example, spin-imbalanced systems, additional independent measurements such as probes of the local spin polarization can be supplemented to fully determine thermodynamic response functions. The spectral response continues to serve as a channel highly sensitive to temperature. Therefore, our spectroscopic thermometry method may be applicable to other quantum gas platforms, including Bose gases, Bose-Fermi mixtures, impurity systems, and Hubbard quantum simulators (55).

REFERENCES AND NOTES

- P. A. Lee, N. Nagaosa, X.-G. Wen, Rev. Mod. Phys. 78, 17–85 (2006).
- M. G. Alford, L. Bovard, M. Hanauske, L. Rezzolla, K. Schwenzer, Phys. Rev. Lett. 120, 041101 (2018).
- A. Adams, L. D. Carr, T. Schäfer, P. Steinberg, J. E. Thomas, New J. Phys. 14, 115009 (2012).
- 4. S. A. Hartnoll, Nat. Phys. 11, 54-61 (2015).
- M. Blake, R. A. Davison, S. Sachdev, Phys. Rev. D 96, 106008 (2017).
- S. Giorgini, L. P. Pitaevskii, S. Stringari, Rev. Mod. Phys. 80, 1215–1274 (2008).
- 7. W. Ketterle, M. W. Zwierlein, Riv. Nuovo Cim. 31, 247 (2008).
- M. W. Zwierlein, Novel Superfluids (Oxford Univ. Press, 2015), pp. 269–422.
- W. Zwerger, in Quantum Matter at Ultralow Temperatures,
 M. Inguscio, W. Ketterle, S. Stringari, G. Roati, Eds.
- (10S Press, 2016), pp. 63–142.
 S. Krinner, T. Esslinger, J.-P. Brantut, J. Phys. Condens. Matter 29, 343003 (2017).
- 11. T.-L. Ho, Phys. Rev. Lett. 92, 090402 (2004).
- M. J. H. Ku, A. T. Sommer, L. W. Cheuk, M. W. Zwierlein, Science 335, 563-567 (2012).
- 13. B. Mukherjee et al., Phys. Rev. Lett. 122, 203402 (2019).
- 14. Z. Yan et al., Phys. Rev. Lett. 122, 093401 (2019).
- 15. L. Tisza, Nature 141, 913 (1938).
- L. Landau, Phys. Rev. 60, 356-358 (1941).
- I. M. Khalatnikov, An Introduction to the Theory of Superfluidity (CRC Press, 1965).
- 18. See supplementary materials.
- 19. P. Hohenberg, P. Martin, Ann. Phys. 34, 291-359 (1965).
- 20. L. P. Kadanoff, P. C. Martin, Ann. Phys. 24, 419-469 (1963).
- 21 L. A. Sidorenkov et al., Nature 498, 78-81 (2013).
- 22. J.-P. Brantut et al., Science 342, 713-715 (2013).
- D. Husmann et al., Proc. Natl. Acad. Sci. U.S.A. 115, 8563–8568 (2018).
- 24. D. K. Hoffmann et al., Nat. Commun. 12, 7074 (2021).
- 24. D. K. Hollmann et al., Nat. Commun. 12, 7074 (2021).
- P. Christodoulou et al., Nature 594, 191–194 (2021).
 T. A. Hilker et al., Phys. Rev. Lett. 128, 223601 (2022).
- 27. X. Li et al., Science **375**, 528–533 (2022).
- 28. S. Gupta et al., Science **300**, 1723–1726 (2003).
- 29. B. Mukherjee et al., Phys. Rev. Lett. 118, 123401 (2017).
- A. Sommer, M. Ku, G. Roati, M. W. Zwierlein, *Nature* 472, 201–204 (2011).
- 31. C. Luciuk et al., Phys. Rev. Lett. 118, 130405 (2017).
- 32. C. Cao et al., Science **331**, 58–61 (2011).
- 33. P. B. Patel et al., Science 370, 1222–1226 (2020).
- 34. Z. Yan et al., Bull. Am. Phys. Soc. 64, Abstract D07.00006 (2019).
- 35. W. B. Hanson, J. R. Pellam, Phys. Rev. 95, 321-327 (1954).
- D. Vollhardt, P. Wölfle, The Superfluid Phases of Helium 3 (Taylor & Francis, 1990).
- 37. C. C. N. Kuhn et al., Phys. Rev. Lett. **124**, 150401 (2020).
- 38. L. Verney, L. Pitaevskii, S. Stringari, Europhys. Lett. 111, 40005 (2015).
- 39. E. Taylor et al., Phys. Rev. A 80, 053601 (2009).
- 40. P. Nozières, S. Schmitt-Rink, J. Low Temp. Phys. 59, 195-211 (1985).

- L. S. Goldner, N. Mulders, G. Ahlers, J. Low Temp. Phys. 93, 131–182 (1993).
- 42. P. C. Hohenberg, B. I. Halperin, Rev. Mod. Phys. 49, 435-479 (1977).
- 43. E. Taylor, Phys. Rev. A 80, 023612 (2009).
- 44. T. Debelhoir, N. Dupuis, Phys. Rev. A 93, 023642 (2016).
- B. Frank, W. Zwerger, T. Enss, Phys. Rev. Res. 2, 023301 (2020).
- P. Patel, "Quantum transport in strongly interacting, ultracold Fermi gases in box potentials," thesis, Massachusetts Institute of Technology (2022).
- X. Wang, X. Li, I. Arakelyan, J. E. Thomas, *Phys. Rev. Lett.* 128, 090402 (2022).
- H. Smith, H. H. Jensen, Transport Phenomena (Clarendon Press, 1989).
 M. A. Escobedo, M. Mannarelli, C. Manuel, Phys. Rev. A 79, 063623 (2009).
- M. W. Zwierlein, C. H. Schunck, C. A. Stan, S. M. F. Raupach, W. Ketterle, *Phys. Rev. Lett.* **94**, 180401 (2005).
- 51. P. Dyke et al., Phys. Rev. Lett. 127, 100405 (2021).
- 52. M. Gring et al., Science 337, 1318–1322 (2012).
- 53. C. Eigen et al., Nature 563, 221-224 (2018).
- M. J. H. Ku, B. Mukherjee, T. Yefsah, M. W. Zwierlein, *Phys. Rev. Lett.* 116, 045304 (2016).
- 55. C. Gross, I. Bloch, Science 357, 995-1001 (2017).
- Z. Yan et al., Replication Data for: Thermography of the superfluid transition in a strongly interacting Fermi gas, version 1, Harvard Dataverse (2023); https://doi.org/10.7910/DVN/KKLTXW.

ACKNOWLEDGMENTS

We thank B. Svistunov, N. Prokofev, W. Zwerger, and in particular the late L. Pitaevskii for illuminating discussions. Funding: This work was supported by the NSF (Center for Ultracold Atoms Award Nos. PHY-1734011 and PHY-2012110), the Air Force Office of Scientific Research (FA9550-16-1-0324 and MURI Quantum Phases of Matter FA9550-14-1-0035), the Office of Naval Research (NO0014-17-1-2257), and the Vannevar Bush Faculty Fellowship (ONR No. N00014-19-1-2631). Author contributions: Z.Y., P.B.P., B.M., and R.J.F. contributed to building the experimental setup. Z.Y., P.B.P., and R.J.F. performed the measurements, and analyzed the data. All authors contributed to the interpretation of the data and the preparation of the manuscript. Competing interests: The authors declare that they have no competing interests. Data and materials availability: All data shown in this work can be found at Harvard Dataverse (56). License information: Copyright © 2024 the authors, some rights reserved; exclusive licensee American Association for the Advancement of Science. No claim to original US government works. https://www.science.org/about/science licenses-journal-article-reuse

SUPPLEMENTARY MATERIALS

science.org/doi/10.1126/science.adg3430 Materials and Methods

Supplementary Text

Figs. S1 to S10 References (57, 58)

Submitted 28 December 2022; accepted 10 January 2024 10.1126/science.adg3430